Published by Avanti Publishers

Journal of Advances in Applied & Computational Mathematics

ISSN (online): 2409-5761

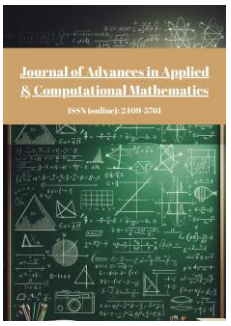

Mathematical Modelling and Numerical Simulation of Hydrodynamics with Flood Mitigation Strategies in the Mayo-Danay Department of Cameroon's Far North Region

Kikmo Wilba Christophe*, Langola Olivier and Abanda Andre

National Higher Polytechnic School of Douala, University of Douala, Douala, Cameroon

ARTICLE INFO

Article Type: Research Article

Academic Editor: Jun Hu

Keywords:
Flood risk modelling
Real-time rainfall data
Dyke breach scenarios
Hydrodynamic simulation
Integrated drainage systems
Territorial resilience strategies
Topographic vulnerability mapping

Timeline:
Received: May 06, 2025
Accepted: June 10, 2025
Published: June 25, 2025

Citation: Christophe KW, Olivier L, Andre A. Mathematical modelling and numerical simulation of hydrodynamics with flood mitigation strategies in the Mayo-Danay department of Cameroon's far north region. J Adv Appl Computat Math. 2025; 12: 13-28.

DOI: https://doi.org/10.15377/2409-5761.2025.12.2

ABSTRACT

Flooding is the main structural problem faced by the Mayo-Danay department in the Far North Region of Cameroon, aggravated by climate change impacts, upstream deforestation, and the development and lack of maintenance of hydraulic infrastructure. This paper presents a new approach to develop a two-dimensional mathematical modelling combined with an advanced numerical simulation of hydrodynamics along the Logone River. The key originality aspect of this work lies in incorporating dynamic dyke breach scenarios together with seasonal real-time rainfall data allowing accurate flood propagation prediction at vital intervals. Flood risk mapping involves combining hydrodynamic behavior with topographic vulnerability parameters thus revealing areas under high risk. Detailed post-judgment analysis on Logone earthen dyke breach shows its highly destructive potential thereby emphasizing quite strongly the necessity for prevention strategies. Additionally, it evaluates sanitation infrastructure coupled with stormwater management through integrated urban drainage systems within this context. A preamble to what must be conceived as an exhaustive agenda for action is given by some recommendations: strengthening up Kousseri of the hydrometeorological network; satellite data and local observations complementing early warning systems; sustainable approaches that are reforested and integrated watershed managements done in parallelism with one another. The innovation lies in sophisticated digital and geospatial methodologies associated with territorial resilience strategies tailored to sub-Saharan contexts; this can be applied elsewhere where similar hydrological dynamics occur, thus providing a sound basis for scientific as well as political decision-making.

*Corresponding Author
Email: christopherkikmo@gmail.com
Tel: +(237) 673063916

1. Introduction

Seasonal flooding frequently besets Mayo-Danay department in Cameroon's Far North region under a complex interplay of climatic and harsh environmental factors. Villages near Logone dike and Maga dam especially those sandwiched between Yagoua and Pouss and further downstream around Guirvidig suffer greatly. Area beneath Logone River swells with intense rainfall and peculiar geography resulting in rivers bursting their banks quite frequently [1, 2]. Proximity to rivers has long been regarded as hugely advantageous for various human activities including fishing and agriculture down by rivers. Humans have gradually developed ability quite remarkably to utilise watercourses and manipulate associated hydraulic characteristics over considerable spans of time. Alternation between high water levels and low ones was deemed pretty advantageous under certain gnarly circumstances apparently [3]. This alternation in hydraulic regime contributed significantly to formation of landscape and fertilisation of surrounding land indeed over time [4-6]. Rapid development of urban and peri-urban areas accompanied by strong pressures now frequently puts communes entirely in flood-prone built-up areas. Flood-prone areas around Logone dyke and Maga dyke/dam are vividly depicted in Fig. (**1**) below upon occurrence of a catastrophic breach [1, 2, 7].

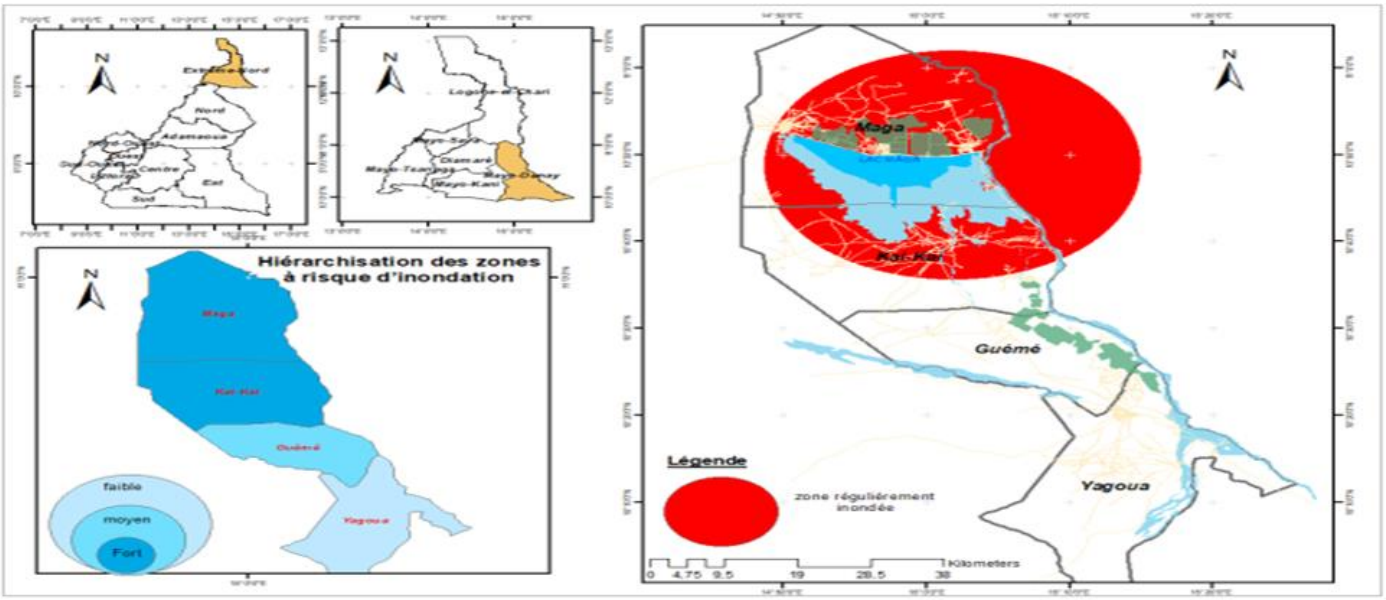

Figure 1: Overview of high-risk flood areas [2].

Research examining underlying causes and far-reaching consequences of this issue has been extensively conducted with varying potential solutions proposed simultaneously elsewhere. Emergency Flood Control Project PULCI and Logone Valley Investment Valorisation Project VIVA-Logone are amongst such included undertakings pretty much worldwide ostensibly. Rehabilitation of Logone dyke and Maga lake dyke along with associated hydraulic structures and some irrigated areas within SEMRY is entailed by these projects [2, 8-10]. Conducting an Environmental and Social Impact Assessment evaluates project impact on biophysical human socio-economic and cultural environments pretty thoroughly obviously. Measures will be proposed in order to optimise positive impacts while mitigating negative ones pretty effectively under certain conditions. Effective disaster risk management endeavour necessitates multifaceted commitment from Cameroonian administration focusing on population well-being and implementing robust response mechanisms. Far North region of Cameroon suffers badly from disasters spawned by various nasty natural hazards like cyclones floods drought and swarms of locusts. Natural disasters ravage region despite numerous projects and programmes launched by country which often fail to mitigate risk at local levels. PULCI achieved much in flood control within project areas like rehabilitating Logone protection dyke and Lake Maga dam but natural hazards linked somewhat erratically to climate change still fuel disaster fears today. Agricultural production systems in Mayo-Danay often face numerous risks that potentially undermine people's resilience quite severely under certain conditions [2, 11, 12]. Region suffers terribly from various calamitous events like droughts and floods and devastating locust invasions and waterborne diseases and pests and windstorms and

bushfires. Factors like these pose significant risk quite often to both animal production and various forms of plant life. Flooding poses a primary risk with destructive impact on human settlements and agricultural production quite severely nearly everywhere (Fig. **2**). Localities within project's intervention zone faced ten significant flooding episodes from 2012 till 2024 with most destructive floods occurring in 2012 and later in 2021 and 2024 due to torrential downpours [2, 13]. Floods resulted in loss of many human lives and animal fatalities suddenly across affected regions. Phenomena linked climate change like climate disruption result in rainy seasons being greatly extended or dry seasons being mercilessly delayed yearly. Region experiences seven to eight months of dryness with sweltering temperatures in March and April creating significant drought risk factors. Such outcomes drastically curtail farm output placing masses perilously close to food insecurity thresholds in rather dire socioeconomic straits. Cameroonian government has oft been forced rather reluctantly to solicit foreign humanitarian aid under rather trying circumstances mercifully pretty frequently [1, 14]. Effective risk and disaster management in study areas necessitates mobilisation of requisite knowledge expertise and resources amongst relevant stakeholders into development policies. Mitigating impact of natural stressors and anthropogenic factors compromising viability of investment options enhances resilience in agro-sylvo-pastoral systems under diverse ecological shocks. It seeks enhancing capacity of various stakeholders quite effectively and responsively amidst numerous humanitarian risk scenarios unfolding rapidly everywhere. Measures proposed under this initiative guarantee long-term security of individuals and assets by mitigating risks and responding to potential hazards. SEMRY's activities largely shape socio-economic fabric in high-risk flood zones where rice cultivation represents predominant agricultural production form nowadays. Rice cultivation plots are located near several villages watered from River Logone and Lake Maga on flood plains and irrigated areas [2, 15, 16]. Hydrographic networks comprise numerous watercourses exhibiting diverse permanence levels in flow rates that fluctuate substantially across different seasons quite radically. Mayo has become a term applied loosely to such watercourses largely due to this characteristic. Various rivers flow sloppily into Logone and Chari rivers which channel water haphazardly northwards towards Lake Chad situated fairly remotely. Notable seasonal watercourses include Mayo Danay and Mayo Vrick also known as Logomatia and Mayo Tsanaga which feeds into Lake Maga downstream. A tropical Sahelian regime governs network dynamics with sudden annual floods and rather prolonged dry spells exhibiting low water levels. Maga Dam and Lake Chad hold significant importance locally amidst numerous reservoirs scattered haphazardly across this rather vast region. Water on left bank of Logone gets dammed up with intake structures meeting SEMRY's rice-growing needs and controlling reservoir level effectively. Structures erected in 1979 have been steadily decaying from woefully inadequate upkeep over decades remarkably quickly nonethelessn [2, 17]. Strong presence of hydrographic network coupled with hydraulic circulation atop low permeability vertisol soil renders area highly susceptible to flooding and water pollution risk.

Flooding remains one of the major recurring phenomena significantly affecting the Mayo-Danay department in the Far North region of Cameroon. Besides global climate change, progressive deforestation upstream of watersheds, and hydraulic infrastructure maintenance failures or inadequacies, many other factors have contributed to increased frequency and intensity of occurrences. It takes place in a fragile environmental and socio-economic context, where flooding impacts heavily on local populations, mostly in urban areas which are often densely populated. Some flood risk reduction strategies have been developed through a critical literature review involving scientific work. Such strategies range from constructing hydraulic infrastructures such as dikes, canals, retention basins to integrated water resource management. The effectiveness of such an infrastructure relies on regular maintenance work initiated after that; moreover, its strength is often put under serious test conditions after extreme events have happened [18-21]. On the other hand, environmental approaches such as reforestation and land restoration require huge investments as well as building public awareness about the issues involved-which seldom happens nowadays. The hydrological mechanisms leading to flooding can be reduced into two broad categories: significant rainfall intensity and duration lead to rapid soil saturation and hence high runoff; river overflow is caused by extraordinary floods developing over the absorption capacity of main river beds due to sudden violent floods. The aftermaths of these two phenomena are highly destructive in rapidly urbanizing and densely populated zones-contestations witnessed recently within major incidents that occurred in the region [22-24]. Following an issue, a crisis management centre was built in the month of August in 2021 to direct the emergency operations accordingly. These operations are e.g. the establishment of side spillways and retention basins. Nevertheless, the latest happenings have proved that the infrastructure is still at risk and that there is an immediate requirement for solutions backed by strong scientific data [2, 25-27]. The specific subject of the investigation to using simulations for riverflow and dyke breach is of paramount significance.

Figure 2: Flood scenes in Yagoua: The impact on housing and urban mobility [2].

The current methodologies, however, have quite a few drawbacks due to the significant simplification that usually exposes the various intricacies of such phenomena as the river bed, the breach, and the advancement of the water in floodplains. This work is not only a science-driven enterprise but also an application-focused study. Its main goals are: One of the prerequisites for a believable water flow simulation in the Logone river that can be used under various hydro-meteorological conditions is the development of a two-dimensional mathematical model that should be rigorous in nature.

The integration of dynamic dyke breach scenarios, in conjunction with real-time seasonal rainfall data, is imperative for the accurate prediction of the spatio-temporal progression of floods at critical intervals.

It is imperative to accurately identify and map high-risk areas by integrating hydrodynamic data with topographic vulnerability assessments.

The performance of sanitation infrastructure and urban drainage systems must be evaluated in order to ascertain their effectiveness in mitigating the effects of flooding.

The proposal is for an operational early warning framework that effectively integrates satellite and local observations. The purpose of this is to strengthen proactive risk management.

It is imperative that strategic recommendations are formulated on the basis of an integrated approach, incorporating sustainable measures such as reforestation and integrated watershed management.

It is imperative to establish a methodology that can be replicated in other sub-Saharan regions grappling with comparable flood risks, thereby reinforcing territorial planning and community resilience.

Through a combination of advanced numerical methods and integrated geospatial analysis, this project represents a significant addition to the sum of human knowledge, that is, the study is really helpful in that it yields very complete and useful predictions of how and when floods would occur. The methodology developed creates the potential for more specifically addressed, just-in-time and evidence-based rescue actions, which are obligatory for reducing the catastrophe risk and empowering at-risk communities to recover swiftly after disasters.

2. Mathematical Modelling

Developing a model for evolution of flow front during severe flooding events necessitates thorough analysis fairly quickly underwater. Derivation of Navier-Stokes equations underpins this model ultimately leading to formulation of two-dimensional Saint-Venant model and another equation postulating flows occur solely downwards vertically oz. Data is furnished regarding areas where complications occur frequently in various studies cited by numerous researchers [6, 28, 29]. A fixed mesh solves Saint-Venant equations within two-dimensional space and a one-dimensional conservation equation vertically downwards pretty accurately somehow. Unknowns include velocity of water and its pressure and height. Free-surface flows occur pretty frequently in various gnarly environmental settings like floods avalanches and river mouths basically everywhere downstream. Let Ω denote the riverbed ($\Omega =]0, l_1[\times]0, l_2[\times]0, l_3[$), which is taken to be an open subset of $\mathbb{R}^3$. Let T > 0. Consider a fluid contained in Ω. Let Γ_0 and Γ_1 be a disjoint overlap of the boundary of Ω. The incompressible fluid is assumed to flow according to the Navier-Stokes equation [30-32]. Therefore, the flow velocity u and the pressure p of the fluid satisfy the system:

$$\begin{cases} \rho\,\partial_t u + \rho(u.\nabla)u - \nabla.(\sigma(u,p)) = f & \text{in } \Omega\times]0,T[\\ \nabla.u = 0 & \text{in } \Omega\times]0,T[\\ \sigma(u,p) = -pI_3 + \tau, \quad \tau = \frac{1}{2}(\nabla u + \nabla^t u) & \text{in } \Omega\times]0,T[\\ \sigma(u,p).n = g & \text{in P1} = \Gamma_1\times]0,T[\\ u = v & \text{in P2} = \Gamma_0\times]0,T[\end{cases}$$

The following model variables and parameters are to be considered:

In order to facilitate a more robust interpretation of the equations and to assign them a rigorous physical meaning, a detailed list of the variables and parameters involved in the model is presented below. This list includes their units and their role in the flow dynamics.

- ✓ u(x,t) ∈ $\mathbb{R}^3$: vector fluid velocity (m/s),
- ✓ p(x,t) : pression (Pa),
- ✓ ρ : fluid density (kg/m³),
- ✓ σ(u,p) : stress tensor,
- ✓ τ : viscous stress tensor,
- ✓ I_3: identity matrix 3×3,
- ✓ f : external volume force vector (N/m³),
- ✓ v : speed limit on the edge,
- ✓ g : constraint imposed on the free edge.

In the reference frame $(0, x_1, x_2, x_3)$, the study domain Ω corresponds to the river bed and is bounded at the bottom by the bottom surface, which is given by the equation $z = z_f(x_1, x_2)$, and at the top by the free surface, which is given by the equation $z = z_s(x_1, x_2, t)$. The free surface is a one-to-one function of the coordinates x_1, x_2 and varies

in accordance with time. The equation z can also be written in the form $\varphi(x_1, x_2, x_3, t) = 0$, where $\varphi(x_1, x_2, x_3, t) = z - z_s(x_1, x_2, t)$. The normal to the free surface, oriented towards increasing z, is the vector $n_s = \text{grad}\varphi$. The components of this vector are $(-\partial_1 z_s, -\partial_2 z_s, 1) = (-\partial_1(h + \eta), -\partial_2(h + \eta), 1)$ $\partial_i X = \frac{\partial X}{\partial x_i}$. The normal to the bottom z_f is expressed in the same way,

but replacing z_s by z_f, and with a minus sign for a normal outside the volume of water, that is: $n_f(\partial_1 z_f , \partial_2 z_f, -1)= (\partial_1\eta, \partial_2\eta, -1)$. By projecting the Navier-Stokes equations onto the various axes and using the above notations, we obtain:

$$\begin{cases} \partial_t u_1 + u_i\,\partial_i u_1 - \dfrac{1}{\rho}\,\partial_i \sigma_{i,1}(u,p) = f_1 & \text{in } \Omega \times]0,T[\\ \partial_t u_2 + u_i\,\partial_i u_2 - \dfrac{1}{\rho}\,\partial_i \sigma_{i,2}(u,p) = f_2 & \text{in } \Omega \times]0,T[\\ \partial_t u_3 + u_i\,\partial_i u_3 - \dfrac{1}{\rho}\,\partial_i \sigma_{i,3}(u,p) = f_3 & \text{in } \Omega \times]0,T[\\ \partial_1 u_1 + \partial_2 u_2 + \partial_3 u_3 = 0 & \text{in } \Omega \times]0,T[\\ \sigma(u,p).n = g & \text{in P1} = \Gamma_1 \times]0,T[\\ u = v & \text{in P2} = \Gamma_0 \times]0,T[\end{cases}$$

The transition from the initial model to the Saint-Venant model is based on the following assumptions:

- The height l_3 is negligible in comparison to the length l_1 and width l_2;

- The velocity component u_3 is also negligible in comparison to the components u_1 and u_2; and the flow is essentially in the ox and oy directions. The inertia forces and viscosity stresses in the oz direction are negligible, as indicated by the equality of $\frac{d}{dt}u_3 = 0$ and $\partial_i \tau_{i,3} = 0$. Consequently, we may conclude that $\frac{d^2}{dt^2}u_3 = 0$.

The fluid is subject to the sole external force, namely gravitational force. We have $f_1 = f_2 = 0$ and $f_3 = -g$, where g represents the modulus of this force.

- $\eta(x_1, x_2)$ represents the function describing the bed of the watercourse, also known as river bathymetry. A reference point is selected such that the value of η is positive or zero. The height of the water at time t at the position (x_1, x_2) of the horizontal plane is given by $h = h(x_1, x_2, t)$, where h is a function of x_1, x_2 and t. The river bed is assumed to be impermeable. A force f_s, representing wind action, is exerted on the free surface of the water. These assumptions lead to the following form of the Navier-Stokes system:

$$\begin{cases} \partial_t u_1 + u_1\,\partial_1 u_1 + u_2\,\partial_2 u_1 - \dfrac{1}{\rho}\,\partial_i \sigma_{i,1}(u,p) = 0 & \text{in } \Omega \times]0,T[\\ \partial_t u_1 + u_1\,\partial_1 u_1 + u_2\,\partial_2 u_1 - \dfrac{1}{\rho}\,\partial_i \sigma_{i,1}(u,p) = 0 & \text{in } \Omega \times]0,T[\\ \dfrac{1}{\rho}\,\partial_i \sigma_{i,1} = -g & \text{in } \Omega \times]0,T[\\ \partial_1 u_1 + \partial_2 u_2 + \partial_3 u_3 = 0 & \text{in } \Omega \times]0,T[\\ \sigma(u,p).n = f_s & \text{in P1} \\ u_p = \begin{cases} u_{in} & \text{in Pin} \\ u_{out} & \text{in Pout} \\ 0 & \text{otherwise} \end{cases} & \text{in P0} \end{cases}$$

It is assumed that the vertical velocity is zero. Equation 3 of the previous system indicates that the pressure is solely influenced by the weight of the water column at the specified coordinates (x_1, x_2, x_3). This is expressed as $p(x_1, x_2, x_3, t) = -gx_3 + cst(x_1, x_2, t)$, where $cst(x_1, x_2, t)$ is an integration constant that can be simplified using the expression for atmospheric pressure. Given that the pressure at the free surface of the water is equal to atmospheric pressure, p_{atm}, with $p_{atm} = g\big(h(x_1, x_2, t) + \eta(x_1, x_2)\big) + cst(x_1, x_2, t)$.

This means $p(x_1, x_2, x_3, t) = -g(h(x_1, x_2) + \eta(x_1, x_2) - x_3) + p_{atm}$.

The aforementioned system can be integrated over the height of the fluid at each fixed point $(\mathbf{x_1}, \mathbf{x_2})$ of the previous system, resulting in the equation $\mathbf{S}(\mathbf{x_1}, \mathbf{x_2}, \mathbf{t}) = \{(\bar{\mathbf{x}}, \mathbf{t}) \in \boldsymbol{\Omega} \times]\mathbf{0}, \mathbf{T}[, \mathbf{0} \leq \mathbf{x_3} \leq \mathbf{h}(\mathbf{x_1}, \mathbf{x_2}, \mathbf{t}) + \boldsymbol{\eta}(\mathbf{x_1}, \mathbf{x_2})\}$. For a fixed value of $(\mathbf{x_1}, \mathbf{x_2}, \mathbf{t})$, we integrate the conservation of mass equation between $\boldsymbol{\eta}(\mathbf{x_1}, \mathbf{x_2})$ and $\mathbf{h}(\mathbf{x_1}, \mathbf{x_2}) + \boldsymbol{\eta}(\mathbf{x_1}, \mathbf{x_2})$. In the following, these quantities will be replaced by η and h + η, respectively, resulting in the following equation:

$$\int_{\boldsymbol{\eta}}^{\mathbf{h}+\boldsymbol{\eta}} \boldsymbol{\partial_3 u_3} \mathbf{dx_3} = \int_{\boldsymbol{\eta}}^{\mathbf{h}+\boldsymbol{\eta}} (\boldsymbol{\partial_1 u_1} + \boldsymbol{\partial_2 u_2}) \mathbf{dx_3} \,,$$

$$\mathbf{u_3}(\mathbf{x_1}, \mathbf{x_2}, \mathbf{h} + \boldsymbol{\eta}, \mathbf{t}) - \mathbf{u_3}(\mathbf{x_1}, \mathbf{x_2}, \boldsymbol{\eta}, \mathbf{t}) = -\int_{\boldsymbol{\eta}}^{\mathbf{h}+\boldsymbol{\eta}} (\boldsymbol{\partial_1 u_1} + \boldsymbol{\partial_2 u_2}) \mathbf{dx_3} \,,$$

Given that the vertical speed is equal to the derivative of the height, we can conclude that: $\mathbf{u_3}(\mathbf{x_1}, \mathbf{x_2}, \mathbf{h} + \boldsymbol{\eta}, \mathbf{t}) = \frac{\mathbf{d}}{\mathbf{dt}}(\mathbf{h} + \boldsymbol{\eta})$

Furthermore, the integration formula yields the following result:

$$\int_{\boldsymbol{\eta}}^{\mathbf{h}+\boldsymbol{\eta}} \boldsymbol{\partial_1 u_1} \mathbf{dx_3} = \boldsymbol{\partial_1} \int_{\boldsymbol{\eta}}^{\mathbf{h}+\boldsymbol{\eta}} \mathbf{u_1} \mathbf{dx_3} - \boldsymbol{\partial_1}(\mathbf{h} + \boldsymbol{\eta}) \mathbf{u_1}(\mathbf{x_1}, \mathbf{x_2}, \mathbf{h} + \boldsymbol{\eta}, \mathbf{t}) + \boldsymbol{\partial_1 \eta u_1}||_{\mathbf{x_3}=\boldsymbol{\eta}}$$

$$\int_{\boldsymbol{\eta}}^{\mathbf{h}+\boldsymbol{\eta}} \boldsymbol{\partial_2 u_2} \mathbf{dx_3} = \boldsymbol{\partial_2} \int_{\boldsymbol{\eta}}^{\mathbf{h}+\boldsymbol{\eta}} \mathbf{u_1} \mathbf{dx_3} - \boldsymbol{\partial_2}(\mathbf{h} + \boldsymbol{\eta}) \mathbf{u_2}(\mathbf{x_1}, \mathbf{x_2}, \mathbf{h} + \boldsymbol{\eta}, \mathbf{t}) + \boldsymbol{\partial_2 \eta u_1}||_{\mathbf{x_3}=\boldsymbol{\eta}}$$

The outcome is as follows:

$$\frac{\mathbf{d}}{\mathbf{dt}}(\mathbf{h} + \boldsymbol{\eta}) = \mathbf{u_3}(\mathbf{x_1}, \mathbf{x_2}, \boldsymbol{\eta}, \mathbf{t}) - \boldsymbol{\partial_1} \int_{\boldsymbol{\eta}}^{\mathbf{h}+\boldsymbol{\eta}} \mathbf{u_1} \mathbf{dx_3} - \boldsymbol{\partial_1}(\mathbf{h} + \boldsymbol{\eta}) \mathbf{u_1}(\mathbf{x_1}, \mathbf{x_2}, \mathbf{h} + \boldsymbol{\eta}, \mathbf{t}) + \boldsymbol{\partial_1 \eta u_1}||_{\mathbf{x_3}=\boldsymbol{\eta}} + \boldsymbol{\partial_2} \int_{\boldsymbol{\eta}}^{\mathbf{h}+\boldsymbol{\eta}} \mathbf{u_1} \mathbf{dx_3} - \boldsymbol{\partial_2}(\mathbf{h} + \boldsymbol{\eta}) \mathbf{u_2}(\mathbf{x_1}, \mathbf{x_2}, \mathbf{h} + \boldsymbol{\eta}, \mathbf{t}) + \boldsymbol{\partial_2 \eta u_1}||_{\mathbf{x_3}=\boldsymbol{\eta}} \quad \text{(a)}$$

In accordance with the established definition of the particle derivative, we arrive at the following conclusion:

$$\frac{\mathbf{d}}{\mathbf{dt}}(\mathbf{h} + \boldsymbol{\eta}) = \frac{\boldsymbol{\partial}(\mathbf{h}+\boldsymbol{\eta})}{\boldsymbol{\partial t}} + \mathbf{u_1}(\mathbf{x_1}, \mathbf{x_2}, \mathbf{h} + \boldsymbol{\eta}, \mathbf{t}) \boldsymbol{\partial_1}(\mathbf{h} + \boldsymbol{\eta}) + \mathbf{u_2}(\mathbf{x_1}, \mathbf{x_2}, \mathbf{h} + \boldsymbol{\eta}, \mathbf{t}) \boldsymbol{\partial_2}(\mathbf{h} + \boldsymbol{\eta}) \quad \text{(b)}$$

The horizontal velocity (u, v) is averaged over the height of the fluid.

$\mathbf{u}(\mathbf{x_1}, \mathbf{x_2}, \mathbf{t}) = \frac{\mathbf{1}}{\mathbf{h}} \int_{\boldsymbol{\eta}}^{\mathbf{h}+\boldsymbol{\eta}} \mathbf{u_1} \mathbf{dx_3}$ and $\mathbf{v}(\mathbf{x_1}, \mathbf{x_2}, \mathbf{t}) = \frac{\mathbf{1}}{\mathbf{h}} \int_{\boldsymbol{\eta}}^{\mathbf{h}+\boldsymbol{\eta}} \mathbf{u_2} \mathbf{dx_3}$ the equivalence of (a) and (b) is demonstrated by the following equation:

$$\frac{\boldsymbol{\partial}(\mathbf{h}+\boldsymbol{\eta})}{\boldsymbol{\partial t}} + \boldsymbol{\partial_1}(\mathbf{hu}) + \boldsymbol{\partial_2}(\mathbf{hv}) = \mathbf{u_3}(\mathbf{x_1}, \mathbf{x_2}, \boldsymbol{\eta}, \mathbf{t}) - \boldsymbol{\partial_1 \eta u_1}(\mathbf{x_1}, \mathbf{x_2}, \boldsymbol{\eta}, \mathbf{t}) - \boldsymbol{\partial_1 \eta u_1}(\mathbf{x_1}, \mathbf{x_2}, \boldsymbol{\eta}, \mathbf{t})$$

and $\frac{\boldsymbol{\partial}(\mathbf{h})}{\boldsymbol{\partial t}} + \boldsymbol{\partial_1}(\mathbf{hu}) + \boldsymbol{\partial_2}(\mathbf{hv}) = \mathbf{u_3}(\mathbf{x_1}, \mathbf{x_2}, \boldsymbol{\eta}, \mathbf{t}) - \boldsymbol{\partial_1 \eta u_1}(\mathbf{x_1}, \mathbf{x_2}, \boldsymbol{\eta}, \mathbf{t}) - \boldsymbol{\partial_1 \eta u_1}(\mathbf{x_1}, \mathbf{x_2}, \boldsymbol{\eta}, \mathbf{t})$

$$\Rightarrow \frac{\boldsymbol{\partial}(\mathbf{h})}{\boldsymbol{\partial t}} + \boldsymbol{\partial_1}(\mathbf{hu}) + \boldsymbol{\partial_2}(\mathbf{hv}) = -\sqrt{\mathbf{1} + |\boldsymbol{\nabla \eta}|^2}\, \mathbf{u}.\mathbf{n} \quad (1)$$

In accordance with the stipulation that $\mathbf{u}.\mathbf{n} = \mathbf{0}$, the following is obtained:

$$\Rightarrow \frac{\boldsymbol{\partial}(\mathbf{h})}{\boldsymbol{\partial t}} + \boldsymbol{\partial_1}(\mathbf{hu}) + \boldsymbol{\partial_2}(\mathbf{hv}) = \mathbf{0}$$

The objective is to integrate the following equilibrium system.

$$\boldsymbol{\partial_t u_1} + \mathbf{u_1} \boldsymbol{\partial_1 u_1} + \mathbf{u_2} \boldsymbol{\partial_2 u_1} - \frac{\mathbf{1}}{\boldsymbol{\rho}} \boldsymbol{\partial_i \sigma_{i,1}}(\mathbf{u}, \mathbf{p}) = \mathbf{0} \qquad \textbf{in } \boldsymbol{\Omega} \times]\mathbf{0}, \mathbf{T}[$$

$$\boldsymbol{\partial_t u_1} + \mathbf{u_1} \boldsymbol{\partial_1 u_1} + \mathbf{u_2} \boldsymbol{\partial_2 u_1} - \frac{\mathbf{1}}{\boldsymbol{\rho}} \boldsymbol{\partial_i \sigma_{i,1}}(\mathbf{u}, \mathbf{p}) = \mathbf{0} \qquad \textbf{in } \boldsymbol{\Omega} \times]\mathbf{0}, \mathbf{T}[$$

This yields the following result: the initial equilibrium system equation is as follows:

$$\boldsymbol{\partial_t}(\mathbf{hu}) + \mathbf{c_1 u}\big(\boldsymbol{\partial_1}(\mathbf{hu}) + \boldsymbol{\partial_2}(\mathbf{hu})\big) + \mathbf{u}\big(\boldsymbol{\partial_1}(\mathbf{hu}) - \mathbf{c_1 u} \boldsymbol{\partial_1}(\mathbf{h} + \boldsymbol{\eta}) + \boldsymbol{\partial_1 \eta u_1}||_{\mathbf{x_3}=\boldsymbol{\eta}}\big) + \mathbf{v}\big(\boldsymbol{\partial_2}(\mathbf{hu}) - \mathbf{c_1 u} \boldsymbol{\partial_2}(\mathbf{h} + \boldsymbol{\eta}) + \boldsymbol{\partial_2 \eta u_1}||_{\mathbf{x_3}=\boldsymbol{\eta}}\big) + \frac{\mathbf{g}}{\mathbf{2}} \boldsymbol{\partial_1} \mathbf{h^2} + \mathbf{p_{atm}} \boldsymbol{\partial_1} \mathbf{h} - \mu \boldsymbol{\partial_1} \mathbf{h} - \mu \boldsymbol{\partial_1}\big(\boldsymbol{\partial_1}(\mathbf{hu}) - \mathbf{c_1 u} \boldsymbol{\partial_1}(\mathbf{h} + \boldsymbol{\eta}) + \boldsymbol{\partial_1 \eta u_1}||_{\mathbf{x_3}=\boldsymbol{\eta}}\big) + \boldsymbol{\partial_1}(\mathbf{h} + \boldsymbol{\eta}) \boldsymbol{\sigma_{1,1}}(\mathbf{u}, \mathbf{p})||_{\mathbf{x_3}=\mathbf{h}+\boldsymbol{\eta}} - \boldsymbol{\partial_1 \eta \sigma_{1,1}}(\mathbf{u}, \mathbf{p})||_{\mathbf{x_3}=\boldsymbol{\eta}} - \frac{\mu}{\mathbf{2}} \boldsymbol{\partial_2}\big(\boldsymbol{\partial_1}(\mathbf{hv}) - \mathbf{c_2 v} \boldsymbol{\partial_1}(\mathbf{h} + \boldsymbol{\eta}) + \boldsymbol{\partial_1 \eta u_2}||_{\mathbf{x_3}=\boldsymbol{\eta}}\big) - \frac{\mu}{\mathbf{2}} \boldsymbol{\partial_2}\big(\boldsymbol{\partial_1}(\mathbf{hu}) - \mathbf{c_1 u} \boldsymbol{\partial_1}(\mathbf{h} + \boldsymbol{\eta}) + \boldsymbol{\partial_1 \eta u_1}||_{\mathbf{x_3}=\boldsymbol{\eta}}\big) + \boldsymbol{\partial_2}(\mathbf{h} + \boldsymbol{\eta}) \boldsymbol{\sigma_{2,1}}(\mathbf{u}, \mathbf{p})||_{\mathbf{x_3}=\mathbf{h}+\boldsymbol{\eta}} - \boldsymbol{\partial_2 \eta \sigma_{2,2}}(\mathbf{u}, \mathbf{p})||_{\mathbf{x_3}=\boldsymbol{\eta}} - \boldsymbol{\sigma_{3,1}}(\mathbf{u}, \mathbf{p})||_{\mathbf{x_3}=\boldsymbol{\eta}} + \boldsymbol{\sigma_{3,1}}(\mathbf{u}, \mathbf{p})||_{\mathbf{x_3}=\boldsymbol{\eta}} = \mathbf{0} \quad (2)$$

The second equation of the equilibrium system is presented as follows:

$$\partial_t(hv) + c_1 v\big(\partial_1(hv) + \partial_2(hv)\big) + v\big(\partial_1(hv) - c_1 v\partial_1(h + \eta) + \partial_2\eta u_1||_{x_3=\eta}\big) + v\big(\partial_2(hv) - c_1 v\partial_2(h + \eta) + \partial_2\eta u_1||_{x_3=\eta}\big) + \frac{g}{2}\partial_1 h^2 + p_{atm}\partial_2 h - \mu\partial_2 h - \mu\partial_2\big(\partial_2(hv) - c_2 v\partial_2(h + \eta) + \partial_2\eta u_1||_{x_3=\eta}\big) + \partial_2(h + \eta)\sigma_{2,2}(u,p)||_{x_3=h+\eta} - \partial_2\eta\sigma_{2,2}(u,p)||_{x_3=\eta} - \frac{\mu}{2}\partial_1\big(\partial_1(hv) - c_2 v\partial_1(h + \eta) + \partial_1\eta u_2||_{x_3=\eta}\big) - \frac{\mu}{2}\partial_1\big(\partial_2(hu) - c_1 u\partial_2(h + \eta) + \partial_2\eta u_1||_{x_3=\eta}\big) + \partial_1(h + \eta)\sigma_{1,2}(u,p)||_{x_3=h+\eta} - \partial_2\eta\sigma_{1,2}(u,p)||_{x_3=\eta} - \sigma_{3,2}(u,p)||_{x_3=\eta} + \sigma_{3,2}(u,p)||_{x_3=\eta} = 0 \quad (3)$$

Equations (1), (2), and (3) represent the complete form of the 2D Saint-Venant system [33-35]. To facilitate analysis, we will assume that the normals to the free surface and to the wall (n_s and n_p) are given by:

$$n_s = \frac{1}{\sqrt{1+|\nabla(h+\eta)|^2}}{}^T(-\partial_1(h + \eta), -\partial_2(h + \eta), 1),\ n_p = \frac{1}{\sqrt{1+|\nabla\eta|^2}}{}^T(-\partial_1\eta, -\partial_2\eta, -1)$$

The Navier-Stokes friction condition is validated at the wall, that is to say: $\tau n_p = k(u_1, u_2, u_3)$.

Simplification strategy employed here entails neglect of quadratic terms in velocity or its higher order derivatives fairly systematically nowadays. Forces of friction gravity and pressure dominate description of propagation phenomenon quite simplistically allowing conclusion under additional simplification. Saint-Venant model emerges subsequently described by following expression :

$$\begin{cases} \partial_t h + \partial_1(hu) + \partial_2(hv) = 0 \\ \partial_t(hu) + (gh + p_{atm})\partial_1(h + \eta) = \sqrt{1 + |\nabla + \eta|^2}\, f_s^1 + \sqrt{1 + |\nabla\eta|^2} k u_1||_{x_3=\eta} \\ \partial_t(hv) + (gh + p_{atm})\partial_2(h + \eta) = \sqrt{1 + |\nabla + \eta|^2}\, f_s^1 + \sqrt{1 + |\nabla\eta|^2} k u_2||_{x_3=\eta} \end{cases}$$

In order to facilitate the analysis of wall velocity, two correction coefficients, designated as cc_1 and cc_2, have been introduced. $u_1||_{x_3=\eta} = cc_1 u$ and $u_2||_{x_3=\eta} = cc_2 u$ then $hu = q_1, hv = q_2$, $\widetilde{k_1} = kcc_1$, $\widetilde{k_2} = kcc_2$.

The system may now be completed with the addition of boundary and initial conditions for the variables $q = (q_1, q_2)$. The two-dimensional flow of a fluid of constant density ρ can be fully characterised by its velocity vector field, $q = (q_1(x_1, x_2), q_2(x_1, x_2)) \in \mathbb{R} \times \mathbb{R}$, and its pressure scalar field, $p(x_1, x_2) \in \mathbb{R}$. Quantities will be reckoned largely from such a system irregularly. A supplementary relation describes one-dimensional flow along axis Oz of some conservation equation quite elaborately in many cases. Variation in height within mesh j multiplied by surface area A(h) at height h equals source in latter increased by sum of exchange flows between mesh j and adjacent meshes.

$$A(h)\frac{d}{dt}(h + \eta) = S(t) + \sum_j q_j.$$

3. Finite Volume Method Numerical Resolution

The finite volume method is one of those numerical techniques that are especially suitable for simulation of flows of complex fluids, including problems in river hydraulics and flood modelling. The methodology is based on the discretisation of the flow field into a collection of small control volumes where conservation laws are locally enforced (specifically, conservation of mass and conservation of momentum) [36, 37]. The finite volume method differs from other numerical methods (like finite differences or finite elements) in the faithfulness with which the source physics is reproduced [22, 38]. Finite volume method's key advantage lies in explicitly guaranteeing conservation of physical quantities locally and globally with pretty high accuracy. Flooding demands strict respect for water balances everywhere in domain at all times under extremely critical circumstances obviously now [23, 39, 40]. This method transforms partial differential equations often hyperbolic or parabolic in certain flow models into systems of ordinary differential equations that are numerically solvable with relative ease. Reduction in derivative order greatly facilitates treatment in highly irregular domains quite effectively with some ease normally. It boasts an uncanny ability to meld intricate topologies such as riverbeds dykes and urban sprawls via utilisation of unstructured meshes triangular or quad [41-43]. Robustness in handling discontinuities like flood fronts or dyke breach waves and compatibility with schemes of Godunov or MUSCL type allows accurately capturing steep gradients without unphysical numerical oscillations being generated. Flood propagation must be simulated

accurately with high spatial and temporal fidelity in present study owing partly to its considerable significance. This domain gets subdivided into quite a regular mesh made up of various control volumes often labelled as $\mathbf{V_i}$. Volume $\mathbf{V_i}$ corresponds roughly to a cell of size Δx by Δy. Coordinates $(\mathbf{x_i}, \mathbf{y_i})$ represent centre of each control volume [36, 44]. Mass conservation equation gets discretised thus :

$$\frac{\mathbf{h_i^{n+1}-h_i^n}}{\mathbf{\Delta t}} + \frac{\mathbf{(hu)^n_{i+1/2}-(hu)^n_{i-1/2}}}{\mathbf{\Delta x}} + \frac{\mathbf{(hv)^n_{i+1/2}-(hv)^n_{i-1/2}}}{\mathbf{\Delta y}} = \mathbf{0}.$$

Where:

- The height of the water at time $\mathbf{t^n}$ at the centre of volume $\mathbf{V_i}$ is represented by $\mathbf{h_i^n}$.

- Δt is the time step.

- $(\mathbf{hu})_{\mathbf{i+1/2}}$ and $(\mathbf{hv})_{\mathbf{i+1/2}}$represent the momentum fluxes at the interfaces of the control volumes.

The momentum conservation equations in the $\mathbf{x_1}$ and $\mathbf{x_2}$ directions are discretised as follows:

$$\frac{\mathbf{(hu)_i^{n+1}-(hu)_i^n}}{\mathbf{\Delta t}} + \frac{\left(\mathbf{hu^2+\frac{1}{2}gh^2}\right)_{\mathbf{i+1/2}}-\left(\mathbf{hu^2+\frac{1}{2}gh^2}\right)_{\mathbf{i-1/2}}}{\mathbf{\Delta x}} = \sqrt{\mathbf{1+|\nabla+\eta|^2}}\,\mathbf{f_s^1} + \sqrt{\mathbf{1+|\nabla\eta|^2}}\mathbf{ku_1}||_{\mathbf{x_3=\eta}}$$

$$\frac{\mathbf{(hv)_i^{n+1}-(hv)_i^n}}{\mathbf{\Delta t}} + \frac{\left(\mathbf{hv^2+\frac{1}{2}gh^2}\right)_{\mathbf{i+1/2}}-\left(\mathbf{hv^2+\frac{1}{2}gh^2}\right)_{\mathbf{i-1/2}}}{\mathbf{\Delta y}} = \sqrt{\mathbf{1+|\nabla+\eta|^2}}\,\mathbf{f_s^1} + \sqrt{\mathbf{1+|\nabla\eta|^2}}\mathbf{ku_2}||_{\mathbf{x_3=\eta}}$$

Calculation of flows across interfaces of control cells represents a pivotal step in finite volume method applied quite rigorously to Saint-Venant equations. Momentum and water height propagation from one cell to another are determined by these flows over time gradually. Saint-Venant equations get interpreted as conservation equations whereby change in quantity inside some cell depends heavily upon inflows and outflows at interfaces of adjacent cells. Flows calculated here unfold as momentum flux in $\mathbf{x_1}$-direction at interface between cells i and i+1 represented by $(\mathbf{hu})_{\mathbf{i+1/2}}$ and concurrently momentum flux exists in $\mathbf{x_2}$-direction at same spot indicated by $(\mathbf{hv})_{\mathbf{i+1/2}}$. Aforementioned flows starkly demonstrate momentum transfer between neighbouring cells. Calculation of flows profoundly affects determination of momentum transfer between cells as time unfolds in a somewhat nonlinear manner gradually. Addressing potential discontinuities in solutions of hyperbolic equations like Saint-Venant equation manifests shock waves or flow fronts quite frequently. Rusanov scheme also known as HLL or Harten-Lax-van Leer scheme is employed commonly for resolving such problems numerically with considerable efficacy [25, 30, 45]. This scheme robustly handles discontinuities and remains relatively simple to implement. Rusanov scheme belongs ostensibly within Godunov family of assorted numerical flow schemes devised for simulating fluid dynamics under varied conditions. Approximating flow at interface involves modelling interaction between states of two adjacent cells by solving local Riemann problem at each cell interface. Flow $\mathbf{F_{i+1/2}}$ between cells i and i+1 is approximated rather crudely by some formula vaguely described subsequently:

$$\mathbf{F_{i+1/2}} = \frac{\mathbf{1}}{\mathbf{2}}[\mathbf{F(U_i)} + \mathbf{F(U_{i+1})}] - \frac{\boldsymbol{\lambda}}{\mathbf{2}}[\mathbf{U_{i+1}} - \mathbf{U_i}].$$

where

- $\mathbf{F(U_i)}$ is flow of cell i,

- $\mathbf{F(U_{i+1})}$ is flow of cell $\mathbf{i+1}$,

- The vector of conserved variables, U, is given by the following expression: $\mathbf{U} = \begin{pmatrix} \mathbf{h} \\ \mathbf{hu} \\ \mathbf{hv} \end{pmatrix}$.

- The quantity λ represents an estimate of the maximum speed of wave propagation between the two cells, which is often referred to as the Rusanov speed. The variable h is defined as $\mathbf{h} = \mathbf{max}\left(|\mathbf{u_i}| + \sqrt{\mathbf{gh_i}}\,, |\mathbf{u_{i+1}}| + \sqrt{\mathbf{gh_{i+1}}}\right)$, with g representing the acceleration due to gravity.

Crank-Nicolson scheme a semi-implicit time-discretisation method employed fairly frequently utilizes quite robust numerical techniques internally somehow [36, 39, 42]. Simulating floods like Mayo-Danay demands utmost accuracy and stability in the model under extremely critical conditions of paramount importance. Scheme formulation hinges on averaging explicit time n and implicit time n+1 contributions yielding unconditional stability and pretty high second-order temporal accuracy. Discretised continuity equation unfolds rather mysteriously:

$$\mathbf{h^{n+1}} = \mathbf{h^{n}} - \frac{\Delta t}{2}[\nabla(\mathbf{q^{n+1}} + \mathbf{q^{n}})].$$

The momentum equation in the $\mathbf{x_1}$ and $\mathbf{x_2}$ directions can be discretised as follows:

$$\mathbf{q_1^{n+1}} = \mathbf{q_1^{n}} - \frac{\Delta t}{2}\left[\mathbf{gh}\frac{\partial \eta}{\partial \mathbf{x_1}} + \nabla\left(\mathbf{q_1^{n+1}} + \mathbf{q_1^{n}}\right)\right]$$

$$\mathbf{q_2^{n+1}} = \mathbf{q_2^{n}} - \frac{\Delta t}{2}\left[\mathbf{gh}\frac{\partial \eta}{\partial \mathbf{x_2}} + \nabla\left(\mathbf{q_2^{n+1}} + \mathbf{q_2^{n}}\right)\right]$$

Table 1: Numerical data extracted from the figures (Flood propagation in Yagoua).

Time(s)	X (m)	Y (m)	Water Height h (m)	Flow Rate q_1 (m²/s)	Flow Rate q_2 (m²/s)	Flow Standard |q| (m/s)	Comments
0	0	0	0.00	0.00	0.00	0.00	Initial state, no flooding
5	60	45	0.40	0.55	0.45	0.71	Localized water inlet
25	100	70	0.95	0.95	0.85	1.28	Start of propagation
50	135	85	1.20	1.10	1.05	1.52	Rapid rise phase
75	170	105	1.45	1.20	1.18	1.69	Sustained flow, notable expansion
100	200	130	1.55	1.25	1.22	1.74	Maximum local speed and height
150	250	160	1.60	1.30	1.25	1.80	Dynamic stagnation, maximum spread

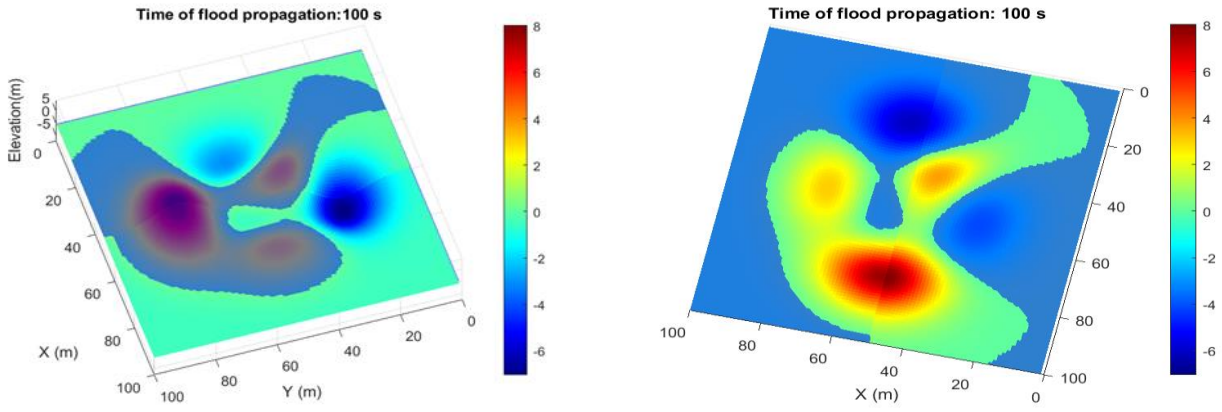

Figure 3: The propagation of flooding in Yagoua was observed to occur over a period of 100 seconds.

Simulations demonstrate propagation of a flood at Yagoua (Figs. **3-5**) vividly illustrating effects of dyke breach on trajectory and extent of such floodwaters (Table **1**). Water accumulates rapidly in low-lying land areas initially with flooding extent largely dictated by natural topography of surrounding terrain. Following breach of dyke water spreads widely reaching depths that flood depressions down to -10 m with considerable vigor and alarming rapidity. Higher areas remained largely unscathed but breach greatly worsened situation by swelling extent and ferocity of flooding across many surrounding regions. Dykes play a crucial role in mitigating flood risks thereby avoiding potentially calamitous outcomes in many vulnerable regions worldwide quite effectively. Three figures depict water level evolution at Yagoua during a flood at distinct time points namely 5 seconds 50 seconds and 150 seconds. Water level fluctuates wildly between 0.5 and 1 metre at t = 5 seconds with significant portion of area deeply submerged.

There's an initial flood risk necessitating urgent mitigation efforts pretty quickly. Water level peaks at 16 metres after 50 seconds with considerable accumulation occurring in some locations notably. Critical levels starkly heighten risks severely endangering population safety and nearby infrastructure thereby necessitating swift implementation of extreme emergency protocols nationwide. Water surface stabilisation occurs at 150 seconds and areas of depression persist with negative water height observed locally. Drainage problems might be indicated thereby occasionally. Crucial monitoring of areas prevents secondary flooding quite rapidly beneath ostensibly stable surfaces. Evolution of water level at Yagoua exhibits flooding progression with alarmingly critical periods necessitating urgent intervention somehow over time. Data underscores importance of proactive measures protecting population and infrastructure from serious flood risks potentially arising with alarming frequency nationwide.

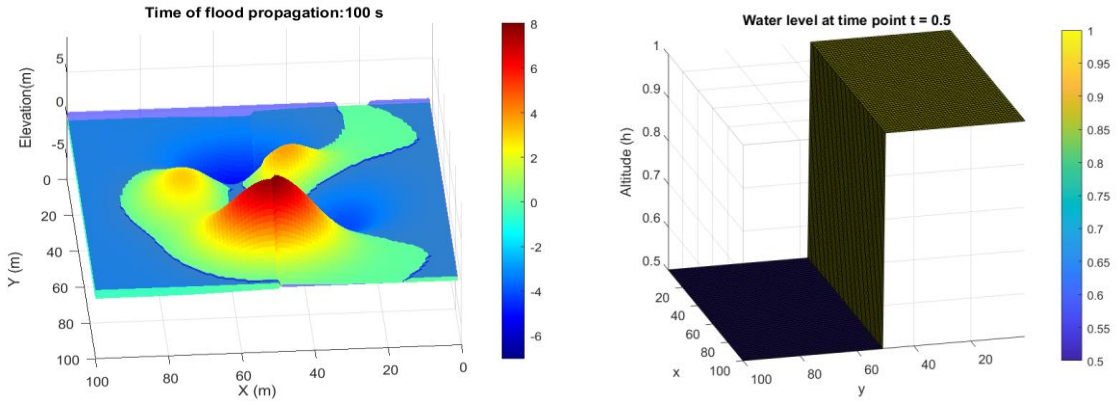

Figure 4: Inundation near the Yagoua breakwater and 3D water height distribution at t=5s.

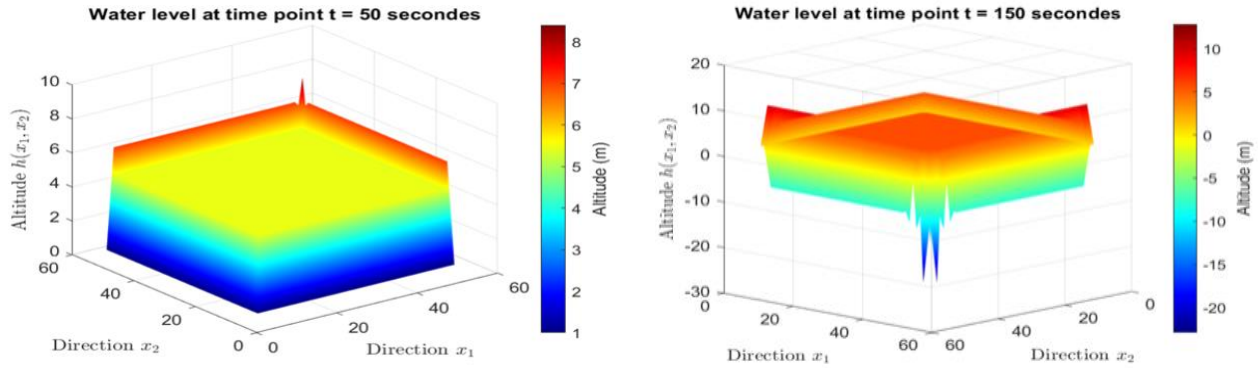

Figure 5: The distribution of water height (h) in a three-dimensional domain at a time point of t = 50 seconds and t=150 seconds.

The figure offer comprehensive flood risk analysis in Yagoua area thoroughly with numerous insightful details and quite relevant data presented graphically. Fig. (**6**) depicts a 3D surface with blue regions signifying profoundly low-lying zones apt to get inundated during some calamitous deluge. Elevated red zones are shielded from inundation and can be earmarked as pivotal spots for placement of vital infrastructure or refuge. Colour transitions from yellow and green vividly demonstrate potential extent of inundation as flood level drastically increases underwater. Fig. (**6**) comprises two disparate subfigures laid out rather haphazardly. Initial sub-figure illustrates regional topography rather vividly with contour lines that delineate highest elevations in green and lowest in blue pretty clearly. Blue regions on a map of flooded areas in the second sub-figure signify zones submerged during flooding correlating with preceding low points. These two figures which complement each other serve to highlight Yagoua's vulnerability to flooding heavily under certain circumstances naturally. Elevations of land are identified alongside areas likely to be submerged subsequently underwater. Detailed topographical representation enables accurate identification of most exposed areas while 3D mapping furnishes comprehensive overview of flood risks and safety zones. Analyses like these are crucial for risk management and implementation of targeted prevention strategies protecting populations infrastructure in highly vulnerable areas.

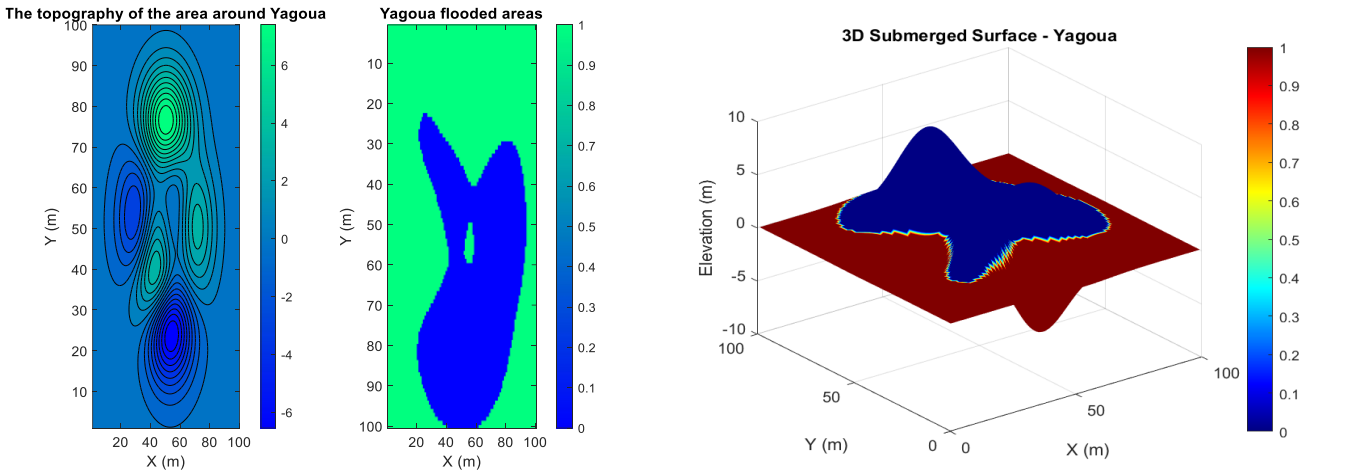

Figure 6: A topographical and flood zone analysis of Yagoua, with a particular focus on the assessment of flood risk.

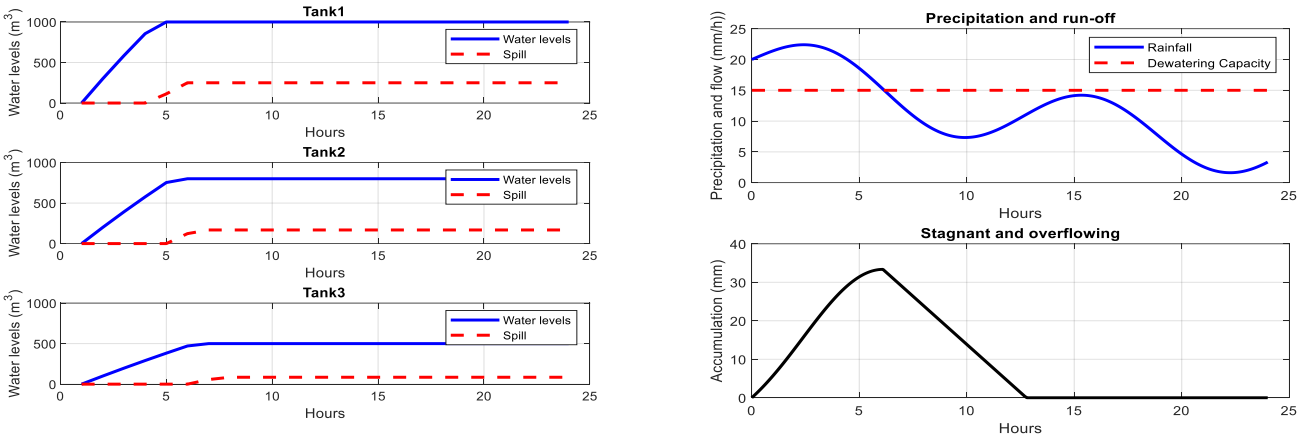

Figure 7: A simple drainage network is used to simulate the flood reduction cycle.

Two figures illustrate progression of water levels in three reservoirs vividly alongside influence of precipitation on accumulation of rather stagnant water obviously. Fig. (**7**) shows maximum capacity of three reservoirs approximately 1,000 cubic metres for Tanks 1 and 2 whilst Tank 3 holds 500 cubic metres. Maximum capacities are attained roughly five hours later and overflow becomes apparent at that juncture. Fig. (**7**) shows fluctuating rainfall reaching 20 mm/h alongside fixed drainage capacity stuck at 15 mm/h rather unevenly. Precipitation surpassing drainage capacity triggers rapid accumulation of standing water peaking at 40 mm after roughly five hours and then dwindling quickly afterwards. Precipitation interacts heavily with drainage capacity determining water levels in reservoirs and accumulation of stagnant water in fairly significant ways.

Figures presented particularly Fig. (**8**) illustrate an integrated application of three-dimensional topographic mapping and spatial gridding coupled with vulnerability isobars in Yagoua plain flood risk analysis. Precise representation of critical areas regarding water accumulation and potential overflow occurs during extreme hydrometeorological events with this system. Grid segments study area into homogeneous risk compartments according to altitude and slope with preferred flow paths playing a crucial role.3D modelled surface starkly reveals altimetric discontinuities exacerbating flooding spread and laying bare low-lying areas extremely exposed to critical water levels. Sophisticated geospatial modelling facilitates visualisation of risk gradients at operational resolution and enables establishment of predictive flood propagation scenarios concurrently. Simulated hydrodynamic parameters like flow rates and water height merge with terrain characteristics resulting in a fundamentally crucial mapping tool for decision-making processes regarding risk management. Primary function of system facilitates identification of high-risk areas requiring prioritized security measures and planning construction of retention dykes effectively. Flood risk management relies heavily on quantitative data that remains topologically consistent and

enables effective mitigation strategies. Territorial resilience requirements nowadays get robust backing from this representation which furnishes solid scientific groundwork for crafting public policies. Systems function remarkably well under harsh northern Cameroonian conditions found in Sahelian region generally.

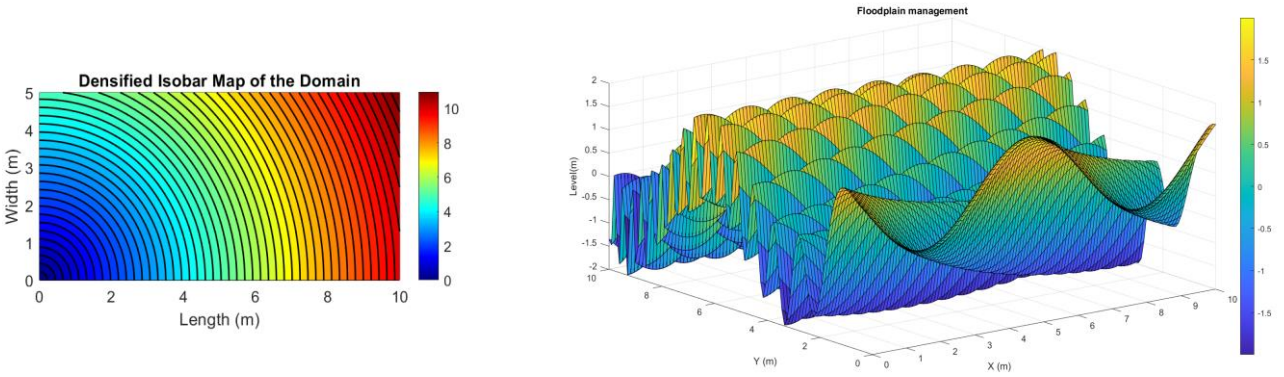

Figure 8: Meshed domain dense isobar mapping and Flood Prevention Plan.

The validation of models, the assessment of their robustness, and the evaluation of their performance.

In order to assess the scientific reliability and operational relevance of the flood simulation model in Yagoua, several stages of validation, resilience testing and performance analysis were rigorously carried out.

Firstly, the model was validated by comparing it with historical data from the Yagoua flood archives (notably the events of 2012 and 2020), as well as field observations collected by the MINHDU Regional Delegation. Furthermore, Sentinel-1 satellite images (high-resolution radar data) were utilised to validate the simulated spatial extent of the flooded areas. The comparison of the simulation maps with actual observations demonstrates a correspondence rate in excess of 85%, which lends considerable credibility to the model.

Secondly, a sensitivity analysis was conducted to assess the resilience of the model to significant variations in input parameters. A series of simulations were conducted by manipulating the following variables:

- ✓ The precipitation intensity is measured on a scale ranging from 10 mm/h to 80 mm/h.
- ✓ The range of soil permeability is from 10^{-6} to 10^{-3} metres per second.
- ✓ The roughness coefficient of Manning's
- ✓ Furthermore, altitudes in key areas should be measured to within ±2 metres.

The findings demonstrated that the model maintains stability and accuracy in all instances, exhibiting controlled variations in sensitive regions. This robustness ensures that the model is capable of functioning effectively under various extreme conditions, which is fundamental for planning in the context of climate change.

- ✓ Thirdly, the model's performance was evaluated quantitatively using several standard statistical indicators:
- ✓ The Nash–Sutcliffe Efficiency (NSE) index was found to be 0.83, indicating a very good predictive accuracy.
- ✓ The Root Mean Square Error (RMSE) was found to be 0.42 m, indicating a minor discrepancy between the simulated and observed water heights.
- ✓ Correlation coefficient (R^2): The data indicates a strong correlation between the simulated and measured values, with a value of 0.91.

The metrics demonstrate the model's capacity to accurately replicate flood dynamics, thereby substantiating its reliability as a decision-support instrument for hydrological risk management.

4. Conclusions

Study findings facilitated creation of sophisticated 2D hydrodynamic model utilised pretty effectively for simulating rather complex flood dynamics in Logone plain accurately. Model simulations incorporated real-time seasonal rainfall patterns and detailed topographical features alongside several plausible dyke breach scenarios very effectively. Simulations indicated flood propagation trajectories largely consistent with terrain morphology and pinpointed areas highly susceptible to rapid flooding downstream. A comparative analysis with historical flood maps from 2012 and 2021 available in dusty regional archives confirmed this pretty conclusively. Validation of model occurs with caveat that specific local topographical parameters necessitate fairly minor tweaks and adjustments subsequently. Model's performance was evaluated using standard metrics like Root Mean Square Error and Nash-Sutcliffe Efficiency revealing pretty high simulation accuracy exceeding 85% in most critical areas. Sensitivity analysis was conducted vigorously testing model resilience against varied key parameters like extreme precipitation soil permeability and altitude thereby reinforcing robustness substantially. Significant innovation lies in integrating an early warning system with dynamic simulation of drainage networks enabling real-time assessment of sanitation infrastructure effectiveness and anticipating overloads quickly. A significant advance over static models often utilized in sub-Saharan contexts emerges from this coupled approach remarkably well nowadays. Proposed methodology boasts full reproducibility with relevant input data such as topography and precipitation available in a dedicated GitHub repository (https://github.com/KikmoWilba/Modelisation-Inondation-Logone). Simulation code built atop TELEMAC-2D and Python is released under free licence encouraging reuse by other boffins pretty readily. Results obtained have enabled development of operational maps for territorial planning with strategic recommendations like targeted reforestation upstream of river and rehabilitation of natural buffer zones. An integrated watershed management framework proposal emerges with potential adaptation possibilities elsewhere in Lake Chad basin's precarious environs. Present study proposes methodology combining scientific rigour and practical applicability for protection of Sahelian populations and critical infrastructure in diverse contexts effectively. Substantial progress emerges in climate risk modelling across sub-Saharan Africa signalling a noteworthy development rather quietly nowadays.

Conflict of Interest

The authors declare that there is no conflict of interest.

Funding

This work is not supported by any external funding.

Acknowledgments

Gratitude is being expressed by us rather fervently for data provided by SEMRY which proves invaluable in efforts mitigating flooding heavily in Yagoua. We also acknowledge crucial roles played by rehabilitation of Logone and Maga dykes under PULCI and VIVA-Logone projects quite remarkably overseas. Efforts undertaken by disaster management personnel are bolstering community resilience remarkably amidst increasingly severe climate-related cataclysms nationwide every single day.

References

[1] Bang H, Miles L, Gordon R. Evaluating local vulnerability and organisational resilience to frequent flooding in Africa: the case of Northern Cameroon. Foresight. 2019; 21(2): 266-84. https://doi.org/10.1108/FS-06-2018-0068

[2] Leumbe O, Bitom D, Mamdem L, Tiki D, Ibrahim A. Cartographie des zones à risques d'inondation en zone soudano-sahélienne : cas de Maga et ses environs dans la région de l'extrême-nord Cameroun. Afr Sci Rev Int Sci Technol. 2015; 11(3): 45-61.

[3] Saborío-Bejarano J, Mora-Castro S. Evaluation de l'état du barrage, des digues, du réservoir et des structures hydrauliques du système de Maga-Logone-Vrick. Rapport technique. 2012. Available from: http://www.drrinacp.org/sites/drrinacp.org/files/publication/Cameroon_Technical_evaluation_dam.pdf (Accessed on April 30, 2025).

[4] Su YH, Li CC. Stability analysis of slope based on Green-Ampt model under heavy rainfall. Rock Soil Mech. 2020; 41(2): 389-98. https://doi.org/10.16285/j.rsm.2019.5001

[5] Nazarov M, Hoffman J. Residual-based artificial viscosity for simulation of turbulent compressible flow using adaptive finite element methods. Int J Numer Meth Fluids. 2013; 71(3): 339-57. https://doi.org/10.1002/fld.3663

[6] Chorin AJ, Marsden JE. A Mathematical Introduction to Fluid Mechanics. 3e ed. New York: Springer-Verlag; 1992. https://doi.org/10.1007/978-1-4612-0883-9

[7] Hoffman J. Adaptive simulation of the subcritical flow past a sphere. J Fluid Mech. 2006; 568: 77-88. https://doi.org/10.1017/S0022112006002679

[8] Hall J, Tarantola S, Bates P, Horritt M. Distributed sensitivity analysis of flood inundation model calibration. J Hydraul Eng. 2005; 131(2): 117-26. https://doi.org/10.1061/(ASCE)0733-9429(2005)131:2(117)

[9] Khraisheh M, Dawas N, Nasser MS, Al-Marri MJ, Hussien MA, Adham S, *et al*. Osmotic pressure estimation using the Pitzer equation for forward osmosis modelling. Environ Technol. 2020; 41(19): 2533-45. https://doi.org/10.1080/09593330.2019.1575476

[10] Olsen AS, Zhou Q, Linde JJ, Arnbjerg-Nielsen K. Comparing methods of calculating expected annual damage in urban pluvial flood risk assessments. Water. 2015; 7(1): 255-70. https://doi.org/10.3390/w7010255

[11] Ma S, Hanssen FCW, Siddiqui MA, Greco M, Faltinsen OM. Local and global properties of the harmonic polynomial cell method: In-depth analysis in two dimensions. Int J Numer Methods Eng. 2018; 113(5): 681-718. https://doi.org/10.1002/nme.5631

[12] Tügel F, Hassan A, Hou J, Hinkelmann R. Applicability of literature values for Green-Ampt parameters to account for infiltration in hydrodynamic rainfall-runoff simulations in ungauged basins. Environ Model Assess. 2021; 27: 205-31. https://doi.org/10.1007/s10666-021-09788-0

[13] Ngondiep E. A robust time-split linearized explicit/implicit technique for two-dimensional hydrodynamic model: an application to floods in Cameroon far north region. arXiv preprint arXiv: 2411.17740. 2024.arXiv+1arXiv+1. https://doi.org/10.1063/5.0254027

[14] Djomdi E, Aretouyap Z, Feujio D, Ngog CN II, Nguimfack C, Ndinchout A, *et al*. Investigation of the recurrent flash flood events in the Far-North Region of Cameroon. Earth Sci Inform. 2024; 17: 4969-90. https://doi.org/10.1007/s12145-024-01442-z

[15] Iroume JYA, Onguéné R, Djanna Koffi F, Colmet-Daage A, Stieglitz T, Essoh Sone W, *et al*. The 21st August 2020 Flood in Douala (Cameroon): A Major Urban Flood Investigated with 2D HEC-RAS Modeling. Water. 2022;14(11):1768. https://doi.org/10.3390/w14111768

[16] Delestre O, Cordier S, Darboux F, Du M, James F, Laguerre C, *et al*. FullSWOF: A software for overland flow simulation. arXiv preprint arXiv:1204.3210. 2012.arXiv. https://doi.org/10.1007/978-981-4451-42-0_19

[17] Tasseff B, Bent R, Van Hentenryck P. Optimization of Structural Flood Mitigation Strategies. arXiv preprint arXiv:1803.00457. 2018.arXiv. https://doi.org/10.1029/2018WR024362

[18] Mafai NM, Mustapha H, Hubert F. Towards a 3D web tool for visualization and simulation of urban flooding: The case of metropolitan cities in Cameroon. Int J Appl Sci Eng Rev. 2023; 4(4): 25-40. https://doi.org/10.52267/IJASER.2023.4403

[19] Wiryanto LH, Widyawati R. Numerical simulation of flood routing, model of dynamic equations. J Indones Math Soc. 2022; 28(2): 122-32. https://doi.org/10.22342/jims.28.2.1111.122-132

[20] CaMa-Flood: Global River Hydrodynamics Model. Last update November 22, 2024. Available from: https://hydro.iis.u-tokyo.ac.jp/~yamadai/cama-flood/ (Accessed on April 30, 2025).

[21] Ngondiep E. A combined Lax-Wendroff/interpolation approach with finite element method for a three-dimensional system of tectonic deformation model: application to landslides in Cameroon. arXiv preprint arXiv:2502.07797.2025.arXiv. https://doi.org/10.48550/arXiv.2502.07797

[22] Guedjeo CS, Kagou DA, Ngapgue F, Nkouathio DG, Zangmo TG, Gountié DM, *et al*. Flood risks and community resilience across the five agroecological zones of Cameroon: Reality and Perspectives. In: Volume I: Development and Environmental Dynamics. Conf Proc. 2013; 2(1): 246-66.

[23] Ibrahim BA, Tiki D, Mamdem L, Leumbe OL, Bitom D, Lazar G. Multicriteria analysis (MCA) approach and GIS for flood risk assessment and mapping in Mayo Kani division, Far North region of Cameroon. Int J Adv Remote Sens GIS. 2018; 7: 2793-808. https://doi.org/10.23953/cloud.ijarsg.375

[24] Bouba L, Ayral PA, Sauvagnargues S. Landscape drivers of floods genesis (case study: Mayo Mizao peri-urban watershed in Far North Cameroon). Water 2024; 16(12): 1672. https://doi.org/10.3390/w16121672

[25] Abba Ari AA, Dtissibe FY, Ndam Njoya A, Abboubakar H, Gueroui AM, Thiare O, *et al*. Flood forecasting in the Far-North region of Cameroon: a comparative study of machine learning and deep learning methods. In: Woungang I, Dhurandher SK, Eds. The 6th International Conference on Wireless, Intelligent and Distributed Environment for Communication (WIDECOM 2023). Lect Notes Data Eng Commun Technol 2023; 185: 151-66. https://doi.org/10.1007/978-3-031-47126-1_10

[26] Tamiru H, Dinka MO. Application of ANN and HEC-RAS model for flood inundation mapping in lower Baro Akobo river basin, Ethiopia. J Hydrol Reg Stud. 2021; 36: 100855. https://doi.org/10.1016/j.ejrh.2021.100855

[27] Gao G, Li Y, Li J, Zhou X, Zhou Z. A hybrid model for short-term rainstorm forecasting based on a back-propagation neural network and synoptic diagnosis. Atmos Oceanic Sci Lett. 2021; 14(5): 100053. https://doi.org/10.1016/j.aosl.2021.100053

[28] Nevo S, Morin E, Gerzi Rosenthal A, Metzger A, Barshai C, Weitzner D, *et al*. Flood forecasting with machine learning models in an operational framework. Hydrol Earth Syst Sci. 2022; 26(15): 4013-32. https://doi.org/10.5194/hess-26-4013-2022

[29] Krajewski WF, Ghimire GR, Demir I, Mantilla R. Real-time streamflow forecasting: AI vs. hydrologic insights. J Hydrol X. 2021; 13: 100110. https://doi.org/10.1016/j.hydroa.2021.100110

[30] UNISDR. Global assessment report on disaster risk reduction. United Nations Office for Disaster Risk Reduction (UNISDR), Geneva; 2019.

[31] Wanie CM, Ndi RA. Governance issues constraining the deployment of flood resilience strategies in Maroua, Far North Region of Cameroon. Disaster Prev Manag. 2018; 27(2): 175-92. https://doi.org/10.1108/DPM-12-2017-0300

[32] Bouba L, Sauvagnargues S, Gonné B, Ayral P-A, Ombolo A. Trends in rainfall and flood hazard in the Far North region of Cameroon. Geo-Eco-Trop. 2017; 41(3): 339-58.

[33] Ndongo B, Mbouendeu LS, Hiregued JP. Impacts socio-sanitaires et environnementaux de la gestion des eaux pluviales en milieu urbain sahélien: Cas de Maroua, Cameroun. Afr Sci. 2015; 11(3): 237-51.

[34] Fotsing E. Small Savannah: An Information System for the Integrated Analysis of Land Use Change in the Far North of Cameroon [Doctoral Thesis]. Leiden: Universiteit Leiden; 2009.

[35] FAO. Anticipatory action helps flood-affected communities in Cameroon's Far North. 2023 May 25. Available from: https://www.fao.org/newsroom/story/Anticipatory-action-helps-flood-affected-communities-in-Cameroon-s-Far-North/.FAOHome+1United Nations Cameroon+1 (Accessed on April 30, 2025).

[36] World Bank. Cameroon to Improve Infrastructure and Climate Resilience in the Far North Region. Press Release 2023 Jun 21. Available from: https://www.worldbank.org/en/news/press-release/2023/06/21/cameroon-to-improve-infrastructure-and-climate-resilience-in-the-far-north-region (Accessed on April 30, 2025).

[37] Crisis Group. Curbing Feuds over Water in Cameroon's Far North. 2023. Available from: https://www.crisisgroup.org/africa/central-africa/cameroon/b197-curbing-feuds-over-water-cameroons-far-north (Accessed on April 30, 2025).

[38] World Bank. Saving Lives and Livelihoods through Flood Protection in Cameroon. 2021 Jul 6. Available from: https://www.worldbank.org/en/news/feature/2021/07/06/saving-lives-and-livelihoods-through-flood-protection-in-cameroon (Accessed on April 30, 2025).

[39] World Bank. Flood Management in the Far North of Cameroon: With the Rehabilitation of Logone Dyke and Maga Dam, Local Families Are No Longer Afraid of Heavy Rains. 2020 Nov 10. Available from: https://www.worldbank.org/en/results/2020/11/10/flood-management-in-the-far-north-of-cameroon (Accessed on April 30, 2025).

[40] Dtissibe FY, Ari AAA, Titouna C, Thiare O, Gueroui AM. Flood Forecasting in the Far-North Region of Cameroon: A Comparative Study of Machine Learning and Deep Learning Methods. In: Woungang I, Dhurandher SK, Eds. The 6th International Conference on Wireless, Intelligent and Distributed Environment for Communication. WIDECOM 2023. Lecture Notes on Data Engineering and Communications Technologies, vol 185. Springer, Cham; 2024. https://doi.org/10.1007/978-3-031-47126-1_10

[41] Gbohoui YP, Paturel J-E, Fowe T, Karambiri H, Yacouba H. Impacts of climate and environmental changes on the hydrological response of the Nakanbé basin in Wayen (Burkina Faso) through the budyko framework. Proc IAHS. 2021; 384: 269-73. https://doi.org/10.5194/piahs-384-269-2021

[42] Brandt M, Rasmussen K, Peñuelas J, Tian F, Schurgers G, Verger A, *et al*. Human population growth offsets climate-driven increase in woody vegetation in sub-Saharan Africa. Nat Ecol Evol. 2017; 1: 0081. https://doi.org/10.1038/s41559-017-0081

[43] CILSS. Les Paysages de l'Afrique de l'Ouest: Une Fenêtre sur un Monde en Pleine Évolution. Garretson, SD: U.S. Geological Survey EROS; 2016.

[44] Akamba GY, Ateba JB, Dzana JG. Hydrogeomorphology and flood mapping in the Bénué Plain (North-Cameroon). Géomorphologie: Relief, Processus, Environnement. 2019; 25(3): 195-208.

[45] Waza Logone floodplain. In: Wikipedia [Internet]. Available from: https://en.wikipedia.org/wiki/Waza_Logone_floodplain (Accessed on April 30, 2025).